Article

Higher Manganese Silicide Nanowires of Nowotny Chimney Ladder Phase

Jeremy M. Higgins, Andrew L. Schmitt, Ilia A. Guzei, and Song Jin

J. Am. Chem. Soc., **2008**, 130 (47), 16086-16094 • DOI: 10.1021/ja8065122 • Publication Date (Web): 05 November 2008

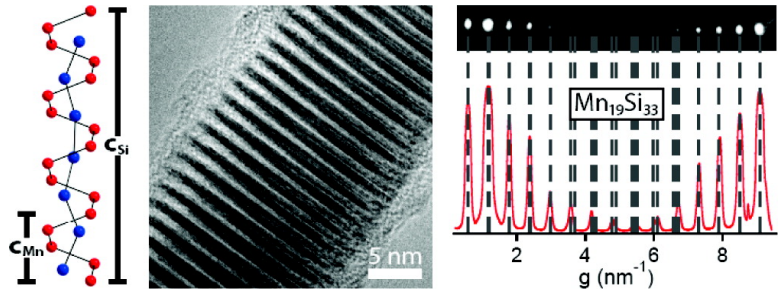

More About This Article

Additional resources and features associated with this article are available within the HTML version:

- Supporting Information
- Access to high resolution figures
- Links to articles and content related to this article
- Copyright permission to reproduce figures and/or text from this article

View the Full Text HTML

J|A|C|S
ARTICLES

Published on Web 11/05/2008

Higher Manganese Silicide Nanowires of Nowotny Chimney Ladder Phase

Jeremy M. Higgins, Andrew L. Schmitt, Ilia A. Guzei, and Song Jin*

Department of Chemistry, University of Wisconsin-Madison, 1101 University Avenue, Madison, Wisconsin 53706

Received August 16, 2008; E-mail: jin@chem.wisc.edu

Abstract: We report the synthesis, structural identification, and electrical properties of the first one-dimensional (1-D) nanomaterials of a semiconducting higher manganese silicide ($MnSi_{2-x}$) with widths down to 10 nm via chemical vapor deposition of the single-source precursor $Mn(CO)_5SiCl_3$. The complex Nowotny chimney ladder structure of these homologous higher manganese silicides, also referred to as Mn_nSi_{2n-m}, $MnSi_{1.75}$, or $MnSi_{1.8}$, contributes to the excellent thermoelectric performance of the bulk materials, which would be enhanced by phonon scattering due to 1-D nanoscale geometry. The morphology, structure, and composition of $MnSi_{2-x}$ nanowires and nanoribbons are examined using electron microscopy and X-ray spectroscopy. Elaborate select area electron diffraction analysis on single-crystal nanowires reveals the phase to be $Mn_{19}Si_{33}$, one of a series of crystallographically distinct higher manganese silicides that have a Nowotny chimney ladder structure. Electrical transport study of single nanowires shows that they are degenerately doped with a low resistivity (17 mΩ·cm) similar to the bulk.

Introduction

The transition metal silicides (TMS) are an interesting class of refractory intermetallic compounds with a wide variety of technologically and scientifically important physical properties. They are ubiquitous in modern CMOS technology as contact and interconnect materials[1] and have potential technological applications in many other important research areas including spintronics,[2,3] photovoltaics,[4] and thermoelectrics.[5] Silicides often have complicated phase behavior and complex crystal structures; among them the semiconducting higher manganese silicides (HMS), represented by $MnSi_{2-x}$, $MnSi_{1.75}$, or $MnSi_{1.8}$, are particularly unusual. They are, in fact, a homologous series of crystallographically distinct phases referred to as the Nowotny chimney ladder (NCL) phases (Figure 1).[6] Commonly occurring in a variety of binary and ternary intermetallic compounds, the general NCL structures are composed of one sublattice of transition metal (TM) atoms from groups 4−9 with a β-Sn configuration overlaid with another sublattice of main group (MG) atoms from groups 13, 14, or 15 with a nearly face centered cubic arrangement. This crystal structure can be aptly described as chimneys of transition metal atoms containing spiraling ladders of main group elements, leading to a beautiful structural motif and giving this class of structures their name (Figure 1a,d). In the simplest cases, for example, Mn_4Si_7, the main group element sublattice is the same size as the unit cell, but more generally the sublattice mismatch gives rise to widely varying and often extremely long lattice periods (up to tens of nanometers) along the unique axis of the tetragonal unit cell (Figure 1e). Four distinct commensurate NCL phases of HMS (Mn_4Si_7,[7] $Mn_{11}Si_{19}$,[8] $Mn_{15}Si_{26}$,[9] $Mn_{27}Si_{47}$[10]) have been reported with atomic positions determined with X-ray diffraction. Their unit cell structures are displayed in Figure 1e. Other commensurate phases, including Mn_7Si_{12}, $Mn_{19}Si_{33}$, $Mn_{26}Si_{45}$, and $Mn_{39}Si_{68}$, have been mentioned in X-ray[9] and electron diffraction[11,12] studies. This list of homologous phases, though lengthy, is probably not an exhaustive account of the structural diversity of HMS phases, as incommensurate crystal structures have been posited for NCL phases of other systems[13−15] and there is some evidence for incommensurate structures in HMS phases as well.[11,12] In general, the stability and electrical properties of the NCL compounds depend on the valence

(1) Zhang, S. L.; Ostling, M. *Crit. Rev. Solid State Mater. Sci.* **2003**, *28*, 1–129.
(2) Manyala, N.; Sidis, Y.; DiTusa, J. F.; Aeppli, G.; Young, D. P.; Fisk, Z. *Nat. Mater.* **2004**, *3*, 255–262.
(3) Manyala, N.; Sidis, Y.; DiTusa, J. F.; Aeppli, G.; Young, D. P.; Fisk, Z. *Nature* **2000**, *408*, 616.
(4) Liu, Z.; Wang, S.; Otogawa, N.; Suzuki, Y.; Osamura, M.; Fukuzawa, Y.; Ootsuka, T.; Nakayama, Y.; Tanoue, H.; Makita, Y. *Sol. Energy Mater. Sol. Cells* **2006**, *90*, 276–282.
(5) Vining, C. Thermoelectric Properties of Silicides. In *CRC Handbook of Thermoelectrics*; Rowe, D. M., Ed.; CRC Press: Boca Raton, FL, 1995; pp 277−285.
(6) Nowotny, H. Crystal Chemistry of Transition Metal Defect Silicides and Related Compounds. In *Chemistry of Extended Defects in Non-Metallic Solids*; Eyring, L., O'Keeffe, M., Eds.; North-Holland Publishing Company: Amsterdam, 1970; pp 223−237.
(7) Karpinskii, O. G.; Evseev, B. A. *Khim. Svyaz Poluprov.* **1969**, 267–72.
(8) Schwomma, O.; Preisinger, A.; Nowotny, H.; Wittmann, A. *Monatsh. Chem.* **1964**, *95*, 1527–37.
(9) Flieher, G.; Voellenkle, H.; Nowotny, H. *Monatsh. Chem.* **1967**, *98*, 2173–9.
(10) Zwilling, G.; Nowotny, H. *Monatsh. Chem.* **1973**, *104*, 668–75.
(11) De Ridder, R.; Amelinckx, S. *Mater. Res. Bull.* **1971**, *6*, 1223–34.
(12) Ye, H. Q.; Amelinckx, S. *J. Solid State Chem.* **1986**, *61*, 8–39.
(13) Lu, G.; Lee, S.; Lin, J.; You, L.; Sun, J.; Schmidt, J. T. *J. Solid State Chem.* **2002**, *164*, 210–219.
(14) Rohrer, F. E.; Lind, H.; Eriksson, L.; Larsson, A. K.; Lidin, S. *Z. Kristallogr.* **2000**, *215*, 650–660.
(15) Rohrer, F. E.; Lind, H.; Eriksson, L.; Larsson, A. K.; Lidin, S. *Z. Kristallogr.* **2001**, *216*, 190–198.

10.1021/ja8065122 CCC: $40.75

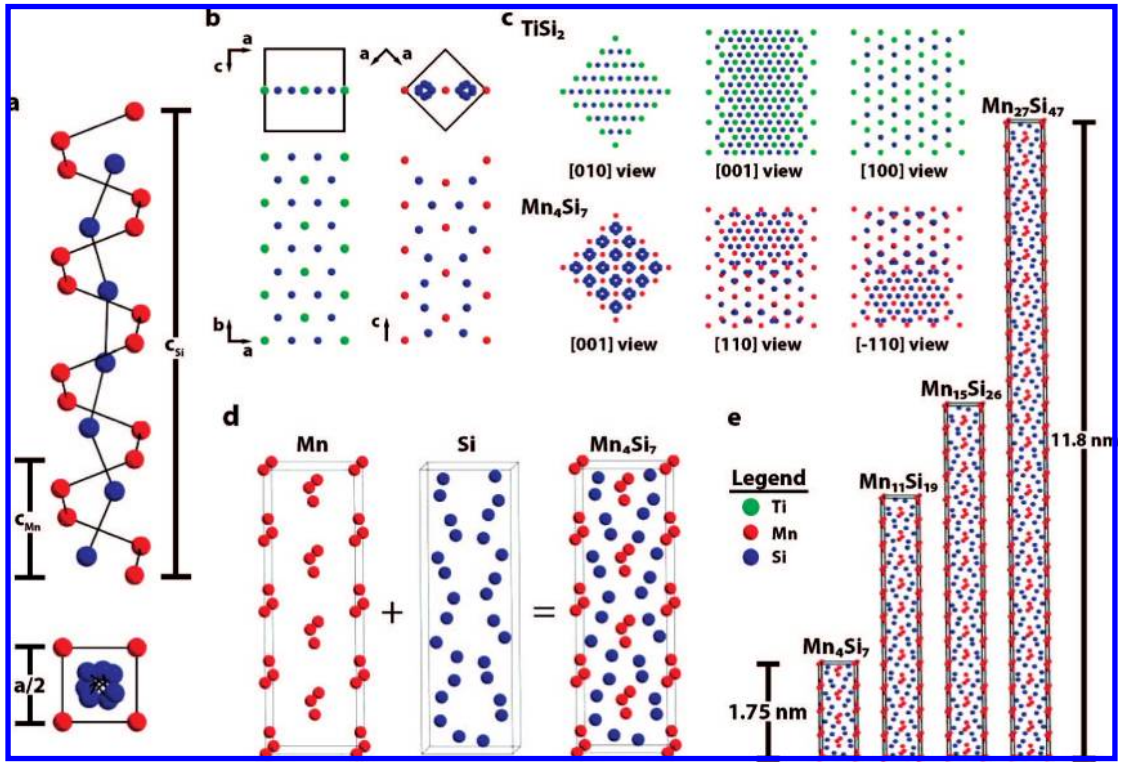

Figure 1. Crystal structures of Nowotny chimney ladder (NCL) phases of manganese silicides and their comparison with the parent $TiSi_2$ structure. (a) Visualization of the NCL structures of $MnSi_{2-x}$ with the Si sublattice (c_{Si}) forming the ladder and the Mn sublattice (c_{Mn}) forming the chimney sublattice. $c_{Si}/c_{Mn} \approx 4$ for reported HMS structures. (b) Comparison of the NCL parent structure $TiSi_2$ (left) clearly showing the 3^6 and 6^3 nets of the stacking planes with the simplest HMS phase, Mn_4Si_7 (right), highlighting the distorted 6^3 nets associated with the defect NCL structure. (c) Comparison of the $TiSi_2$ structure and the Mn_4Si_7 along comparable projections revealing NCL supercell characteristics similar to different rotated views of the $TiSi_2$ supercell. This rotation in cell structure is characteristic of the defect Nowotny chimney ladder structures. (d) General NCL structure formed by combining one sublattice of transition metal atoms with a sublattice of main group atoms. (e) Effects of sublattice periodicity on unit cell size for the four HMS phases completely characterized crystallographically with atomic positions.

electron count (VEC) per transition metal atom;[16] NCL phases with VECs less than 14 (generally transition metals of groups 4, 5, and 6) are metallic, whereas NCL phases having metals from groups 7, 8, and 9 have a VEC of 14 and are semiconducting.[17−19] The NCL phases of the HMS have $13.90 < \text{VEC} \leq 14$ and have been shown to be semiconducting both theoretically and experimentally;[5,20] however, it is unclear if these crystallographically distinct compounds will have significantly different physical properties. Direct and indirect bandgaps ranging from 0.4 to 0.9 eV have been reported for the HMS[21] which may indicate that there are subtle differences in the electronic properties between the different phases.

The higher manganese silicides are good thermoelectric materials with reported figures of merit (ZT) up to 0.7−0.8.[5,22,23] However, most studies are complicated by a large variety and complexity of NCL structures and the subsequent intergrowth of various phases in bulk samples. Thermoelectric materials are evaluated based on their figure of merit $ZT = (S^2\sigma/\kappa)T$, where S is the Seebeck coefficient, σ is the electrical conductivity, κ is the thermal conductivity, and T is the average temperature of measurement. State of the art commercial thermoelectric materials have ZTs near 1, while larger scale commercial applications as either thermoelectric generators or solid state refrigerators will require materials with a ZT greater than 4.[24,25] One development strategy for bulk thermoelectric materials (called the "phonon glass electron crystal" approach)[26,27] focuses on increasing the structural complexity of new materials[25,27] in hopes of limiting phonon conductivity while maintaining normal electron conductivity. A different strategy to enhance the thermoelectric performance uses nanomaterials such as thin film superlattices,[28] nanodot superlattices,[29] nanowires (NWs),[30−32]

(16) Jeitschko, W.; Parthe, E. *Acta Crystallogr.* **1967**, *22*, 417–30.
(17) Fredrickson, D. C.; Lee, S.; Hoffmann, R. *Inorg. Chem.* **2004**, *43*, 6159–67.
(18) Fredrickson, D. C.; Lee, S.; Hoffmann, R.; Lin, J. *Inorg. Chem.* **2004**, *43*, 6151–8.
(19) Imai, Y.; Watanabe, A. *Intermetallics* **2004**, *13*, 233–241.
(20) Nishida, I. *J. Mater. Sci.* **1972**, *7*, 435–40.
(21) Mahan, J. E. *Thin Solid Films* **2004**, *461*, 152–159.
(22) Aoyama, I.; Fedorov, M. I.; Zaitsev, V. K.; Solomkin, F. Y.; Eremin, I. S.; Samunin, A. Y.; Mukoujima, M.; Sano, S.; Tsuji, T. *Jpn. J. Appl. Phys* **2005**, *44*, 8562–8570.
(23) Aoyama, I.; Kaibe, H.; Rauscher, L.; Kanda, T.; Mukoujima, M.; Sano, S.; Tsuji, T. *Jpn. J. Appl. Phys* **2005**, *44*, 4275–4281.
(24) Disalvo, F. J. *Science* **1999**, *285*, 703–706.
(25) Chen, G.; Dresselhaus, M. S.; Dresselhaus, G.; Fleurial, J. P.; Caillat, T. *Int. Mater. Rev.* **2003**, *48*, 45–66.
(26) Slack, G. A. New Materials and Performance Limits for Thermoelectrics Cooling. In *CRC Handbook of Thermoelectrics*; Rowe, D. M., Ed.; CRC Press: Boca Raton, FL, 1995; pp 407−440.
(27) Snyder, G. J.; Toberer, E. S. *Nat. Mater.* **2008**, *7*, 105–114.
(28) Venkatasubramanian, R.; Siivola, E.; Colpitts, T.; O'Quinn, B. *Nature* **2001**, *413*, 597–602.
(29) Harman, T. C.; Taylor, P. J.; Walsh, M. P.; LaForge, B. E. *Science* **2002**, *297*, 2229–2232.
(30) Boukai, A. I.; Bunimovich, Y.; Tahir-Kheli, J.; Yu, J.-K.; Goddard, W. A., III.; Heath, J. R. *Nature* **2008**, *451*, 168–171.
(31) Hochbaum, A. I.; Chen, R.; Delgado, R. D.; Liang, W.; Garnett, E. C.; Najarian, M.; Majumdar, A.; Yang, P. *Nature* **2008**, *451*, 163–167.
(32) Zhou, F.; Szczech, J.; Pettes, M. T.; Moore, A. L.; Jin, S.; Shi, L. *Nano Lett.* **2007**, *7*, 1649–1654.

or nanostructured composites[33] to enhance the surface phonon scattering, resulting in drastically reduced thermal conductivity without significantly affecting the electrical conductivity. For example, it has been reported that *ZT*s are enhanced nearly 100-fold for NWs of silicon, a material not usually considered a "good" thermoelectric.[30,31] These gains have reinvigorated the field, with additional ZT improvements possible due to quantum confinement effects.[34,35] Nanowires of higher manganese silicides ($MnSi_{2-x}$) having both a complex NCL phase and 1-D geometry would converge both of these research approaches. While the *ZT* of thermoelectric $MnSi_{2-x}$ materials should be greatly improved from its already good bulk values, such semiconducting nanowires of the unique and complex NCL phase are fascinating model systems for the investigation of phonon confinement and transport.

The complexity of the silicide materials makes the synthesis of their nanomaterials generally more difficult than commonly reported prototypical semiconductors.[36,37]

Successful synthesis of complex intermetallic silicide nanowires (NWs) requires control over the vapor phase delivery of both the transition metal and silicon elements as well as anisotropic one-dimensional growth. We have developed two complementary approaches to the synthesis of silicide NWs based upon the chemical vapor deposition (CVD) of organometallic single source precursors (SSPs),[38−41] which contain both silicon and the transition metal of interest, along with chemical vapor transport (CVT) of silicide materials.[42−44] In this paper, we report the synthesis and characterization of the single source precursor $Mn(CO)_5SiCl_3$. Using this SSP, free-standing nanowires and nanoribbons of higher manganese silicide were synthesized via chemical vapor deposition and then characterized with electron microscopy and spectroscopy. Elaborate electron diffraction analysis allowed the direct identification of the HMS phase as $Mn_{19}Si_{33}$, which is the first nanowire example of any Nowotny chimney ladder phase to our knowledge. The electrical properties of thermoelectric $Mn_{19}Si_{33}$ nanowires are also discussed.

Experimental Section

Synthesis of $Mn(CO)_5SiCl_3$. The synthesis procedure was modified from literature.[46] In a typical reaction, $SiHCl_3$ (Aldrich, 15 mL, 150 mmol) and $Mn_2(CO)_{10}$ (Aldrich, 2.954 g, 7.576 mmol) were loaded into a thick-wall glass Carius tube equipped with a Teflon valve and pumped down to 0.5 Torr. The sealed vessel was then heated to 130 °C under stirring for 4 days during which the color of the yellow solution lightened and a white precipitate was observed. *Warning: Heating a volatile liquid reaction mixture that generates gas in closed containers can cause pressure buildup and potential explosion!* After cooling, excess $SiHCl_3$ was removed via gravity filtration in an inert atmosphere, and the resulting solid product mixture was transferred into a sublimation apparatus in a nitrogen filled glovebox. The solid was dried under vacuum and sublimed at 70 °C and 100 mTorr for 3 h before the product was collected from the coldfinger of the sublimation apparatus inside a glovebox. The final yellow-tinged white solid product weighed 3.114 g (62.4% yield). IR (KBr pellet): 2129 (s), 2021 (s) cm^{-1}.[45]

Single Crystal X-Ray Crystallography of $Mn(CO)_5SiCl_3$. Single crystals suitable for X-ray crystallography were grown by slow evaporation from a concentrated solution of the product in dichloromethane in the glovebox. A colorless crystal with approximate dimensions $0.46 \times 0.27 \times 0.24$ mm^3 was selected for a single-crystal diffraction experiment. The crystal proved to be a nonmerohedral twin with two components (9:2 ratio) related by a 180° rotation about [100]. The refinement results are reported for the major component. The final least-squares refinement of 271 parameters against 4051 data resulted in residuals *R* (based on F^2 for $I \geq 2\sigma$) and *wR* (based on F^2 for all data) of 0.0264 and 0.0725.[46] See full details of crystal structure solution in the Supporting Information.

Growth of $Mn_{19}Si_{33}$ Nanowires. $Mn_{19}Si_{33}$ nanowires were synthesized in a home-built chemical vapor deposition setup comprised of a quartz tube heated by a tube furnace and equipped with pressure and gas flow controls. 100 mg of $Mn(CO)_5SiCl_3$ placed in an alumina boat were sublimed at the upstream end of the tube furnace at 150 °C and carried downstream by a flow of 150 sccm of argon. Growth substrates of silicon chips were placed in the hot zone of the heated tube. Typically, the reaction was carried out at 700 °C and 200 Torr for 10−15 min.

Nanowire Characterization. Scanning electron microscopy (SEM) was carried out with an LEO Supra FESEM using as-grown substrates. NWs were sonicated and suspended in ethanol and dispersed onto lacey carbon film TEM grids for energy dispersive X-ray spectroscopy (EDS) analysis and HRTEM imaging. EDS analysis of single NWs was completed on a Zeiss 1500XB CrossBeam Workstation equipped with a nitrogen cooled Thermo Electron Corp. Si(Li) detector using 15 kV excitation beams. Analysis of EDS spectra was completed using the Noran software package. High resolution transmission electron microscopy (HRTEM) imaging of NWs was carried out on a Philips CM200 UT TEM with an accelerating voltage of 200 kV. Selected area electron diffraction (SAED) patterns were collected on image plates using focal lengths between 750 mm and 1.95 m and calibrated against a polycrystalline aluminum standard.

Electrical Device Fabrication and Measurements. For device fabrication, HMS NWs were first suspended in ethanol via sonication and deposited onto degenerately doped Si(100) substrates coated with 600 nm of thermally grown silicon oxide. Electrodes were then defined using e-beam lithography, and nonmagnetic metal contacts to NWs were made using e-beam evaporated 50 nm Au atop 50 nm Ti after a 7 s buffered HF etch (buffered HF improved, Transene Inc.). Room temperature resistivity measurements were made on a computer controlled probe station using a DAQ card and current preamplifier. Low temperature measurements were performed on Al wire-bonded device chips using a Quantum Design Physical Property Measurement System (PPMS) and a Keithley 2400 sourcemeter controlled with National Instruments Labview software.

Results and Discussion

Synthesis and Characterization of Single Source Precursor. Most nanowires synthesized to date have relied on the simple eutectic phase behavior of vapor−liquid−solid (VLS) growth

(33) Poudel, B.; Hao, Q.; Ma, Y.; Lan, Y.; Minnich, A.; Yu, B.; Yan, X.; Wang, D.; Muto, A.; Vashaee, D.; Chen, X.; Liu, J.; Dresselhaus, M. S.; Chen, G.; Ren, Z. *Science* **2008**, *320*, 634–638.
(34) Hicks, L. D.; Dresselhaus, M. S. *Phys. Rev. B: Condens. Matter Mater. Phys.* **1993**, *47*, 16631–4.
(35) Hicks, L. D.; Dresselhaus, M. S. *Phys. Rev. B: Condens. Matter Mater. Phys.* **1993**, *47*, 12727–31.
(36) Law, M.; Goldberger, J.; Yang, P. *Annu. Rev. Mater. Res.* **2004**, *34*, 83–122.
(37) Xia, Y.; Yang, P.; Sun, Y.; Wu, Y.; Mayers, B.; Gates, B.; Yin, Y.; Kim, F.; Yan, H. *Adv. Mater.* **2003**, *15*, 353–389.
(38) Schmitt, A. L.; Bierman, M. J.; Schmeisser, D.; Himpsel, F. J.; Jin, S. *Nano Lett.* **2006**, *6*, 1617–1621.
(39) Schmitt, A. L.; Higgins, J. M.; Jin, S. *Nano Lett.* **2008**, *8*, 810–815.
(40) Schmitt, A. L.; Jin, S. *Chem. Mater.* **2007**, *19*, 126–128.
(41) Schmitt, A. L.; Zhu, L.; Schmeisser, D.; Himpsel, F. J.; Jin, S. *J. Phys. Chem. B* **2006**, *110*, 18142–6.
(42) Song, Y.; Schmitt, A. L.; Jin, S. *Nano Lett.* **2007**, *7*, 965–9.
(43) Szczech, J. R.; Schmitt, A. L.; Bierman, M. J.; Jin, S. *Chem. Mater.* **2007**, *19*, 3238–3243.
(44) Song, Y.; Jin, S. *Appl. Phys. Lett.* **2007**, *90*, 173122/1–173122/3.
(45) Novak, I.; Huang, W.; Luo, L.; Huang, H. H.; Ang, H. G.; Zybill, C. E. *Organometallics* **1997**, *16*, 1567–1572.
(46) Sheldrick, G. M. *Acta Crystallogr., Sect. A* **2008**, *A64*, 112–122.

to obtain the nanowires of interest.[36,47] However, when intermetallic compounds with high melting points and more complicated phase behavior, such as silicides, are desired in nanowire form, effective delivery of precursor can be challenging. We have developed a single source precursor (SSP) strategy that incorporates both metal and silicon elements into a single, volatile organometallic molecule for vapor phase delivery in CVD growth. Using this strategy we have successfully synthesized a number of transition metal silicide NWs.[38−41] Other recent examples of metal silicide NW syntheses have focused on the delivery of only one of the silicide's elemental components, either metal or silicon, while relying on growth substrates to provide the other elemental component.[48−59]

We have found that metal carbonyl-silyl organometallic molecules of $TM(CO)_x(SiCl_3)_y$ (TM = Fe, Co, Mn so far; x = 4, 5; y = 1, 2) work well as SSPs for CVD synthesis of TMS nanowires. They readily sublime or evaporate after melting at modest temperature (100−150 °C) to allow controllable vapor phase delivery and undergo thermal decomposition to metals and silicon at higher temperatures (usually >400 °C). The carbonyl ligands are labile and dissociate upon thermal decomposition of the SSP. The complexes have relatively strong TM−Si bonds which allow vapor phase delivery of metal and silicon to the growth substrate. These compounds are readily synthesized by reacting commercially available metal carbonyl clusters with $SiHCl_3$ via an oxidative addition−elimination reaction and purified using sublimation.[45] The reaction for the SSP used in this study, $Mn(CO)_5SiCl_3$, is shown in Figure 2a.

Once synthesized and purified via sublimation, the SSP was characterized via infrared spectroscopy and X-ray crystallography. The IR spectra of precursor in a KBr pellet was in good agreement with literature reports.[45] Additionally, the precursor was recrystallized in dichloromethane, and its chemical identity and molecular structure are unequivocally confirmed by single-crystal X-ray diffraction (Table 1). Incidentally, the crystal structure of this compound has not been reported in the literature so far. A molecular drawing of SSP molecule $Mn(CO)_5SiCl_3$ derived from the X-ray diffraction analysis (Figure 2b) show that the ligands have a slightly distorted octahedral arrangement. The average Mn−Si bond length is 2.352(2) Å, whereas the Mn−C bond lengths range between 1.866(3) and 1.875(2) Å with an average of 1.869(6) Å and no statistically significant difference between the *trans*- and *cis*-CO ligands.

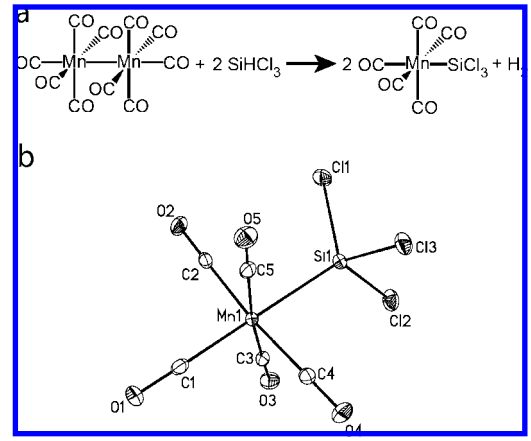

Figure 2. (a) Synthesis of single source precursor (SSP) $Mn(CO)_5SiCl_3$. (b) A molecular drawing of $Mn(CO)_5SiCl_3$ shown with 50% thermal probability ellipsoids.

Table 1. X-Ray Data Collection and Structure Refinement Parameters for $Mn(CO)_5SiCl_3$

crystal system	monoclinic
space group	$P2_1/c$
a (Å)	13.7643(5)
b (Å)	12.5749(4)
c (Å)	12.7096(4)
β (deg)	96.977(2)
volume	2183.55(13) Å^3
Z	8
density (calculated)	2.004 g/cm^3
Data Collection and Reduction	
T (K)	102 (2)
λ (Å)	1.541 78
data/restraints/parameters	4051/0/271
R(obs), R(all)	0.0264, 0.0301
R_w(obs), R_w(all)	0.0696, 0.0725
GoF on F^2	0.911
largest diff peak/hole	0.401 and −0.564 e·Å^{-3}

Nanowire Synthesis, Morphology, and Composition. $Mn(CO)_5SiCl_3$ was used to synthesize nanowires of $MnSi_{2-x}$ using a home-built CVD system shown schematically in Figure 3a. $Mn(CO)_5SiCl_3$ allows effective vapor delivery of Mn and Si, but some mechanism for promoting anisotropic one-dimensional nanowire growth is also required. Our previous experience[38,40,41] showed that a thin layer of SiO_2 (1−2 nm) on a Si substrate is sufficient to accomplish this task for many silicide NWs; however in the case of $MnSi_{2-x}$ NW growth such an oxide layer appeared to be unnecessary. Additionally, the volatilization behavior of $Mn(CO)_5SiCl_3$ was somewhat different from that of $Fe(CO)_4(SiCl_3)_2$ and $Co(CO)_4SiCl_3$ SSPs for CVD growth of FeSi and CoSi NWs.[38,41] Under the growth conditions used here $Mn(CO)_5SiCl_3$, a fine powder, sublimed rather than melted during the reaction and required a slightly higher temperature for proper volatilization. The reactions more sensitively depend on the SSP sublimation temperature as dictated by the position of the precursor boats relative to the hot zone of the furnace.

As-grown substrates were examined using SEM revealing mixed nanowire and nanoribbon morphologies (Figure 3b−d). A mixture of long nanowires and nanoribbons, clearly seen in Figure 3b, with microns to tens of microns lengths and 10−100 nm widths were observed in relatively low density. The nanoribbons have thickness much smaller than their width, which is only apparent on the as grown substrates due to their twist. In addition to these relatively large nanostructures, shorter (~1 μm) nanorods with a smaller diameter of 10−20 nm and

(47) Morales, A. M.; Lieber, C. M. *Science* **1998**, *279*, 208–211.
(48) Seo, K.; Varadwaj, K. S. K.; Mohanty, P.; Lee, S.; Jo, Y.; Jung, M. H.; Kim, J.; Kim, B. *Nano Lett.* **2007**, *7*, 1240–1245.
(49) Chueh, Y. L.; Ko, M. T.; Chou, L. J.; Chen, L. J.; Wu, C. S.; Chen, C. D. *Nano Lett.* **2006**, *6*, 1637–1644.
(50) Dong, L.; Bush, J.; Chirayos, V.; Solanki, R.; Jiao, J.; Ono, Y.; Conley, J. F.; Ulrich, B. D. *Nano Lett.* **2005**, *5*, 2112–2115.
(51) In, J.; Varadwaj, K. S. K.; Seo, K.; Lee, S.; Jo, Y.; Jung, M. H.; Kim, J.; Kim, B. *J. Phys. Chem. C* **2008**, *112*, 4748–4752.
(52) Kang, K.; Kim, S. K.; Kim, C. J.; Jo, M. H. *Nano Lett.* **2008**, *8*, 431–436.
(53) Kim, C. J.; Kang, K.; Woo, Y. S.; Ryu, K. G.; Moon, H.; Kim, J. M.; Zang, D. S.; Jo, M. H. *Adv. Mater.* **2007**, *19*, 3637–3642.
(54) Kim, J.; Anderson, W. A. *Thin Solid Films* **2005**, *483*, 60–65.
(55) Kim, J.; Shin, D. H.; Lee, E. S.; Han, C. S.; Park, Y. C. *Appl. Phys. Lett.* **2007**, *90*, 253103/1–253103/3.
(56) Ouyang, L.; Thrall, E. S.; Deshmukh, M. M.; Park, H. *Adv. Mater.* **2006**, *18*, 1437–1440.
(57) Seo, K.; Varadwaj, K. S. K.; Cha, D.; In, J.; Kim, J.; Park, J.; Kim, B. *J. Phys. Chem. C* **2007**, *111*, 9072–9076.
(58) Varadwaj, K. S. K.; Seo, K.; In, J.; Mohanty, P.; Park, J.; Kim, B. *J. Am. Chem. Soc.* **2007**, *129*, 8594–8599.
(59) Yan, X. Q.; Yuan, H. J.; Wang, J. X.; Liu, D. F.; Zhou, Z. P.; Gao, Y.; Song, L.; Liu, L. F.; Zhou, W. Y.; Wang, G.; Xie, S. S. *Appl. Phys. A* **2004**, *79*, 1853–1856.

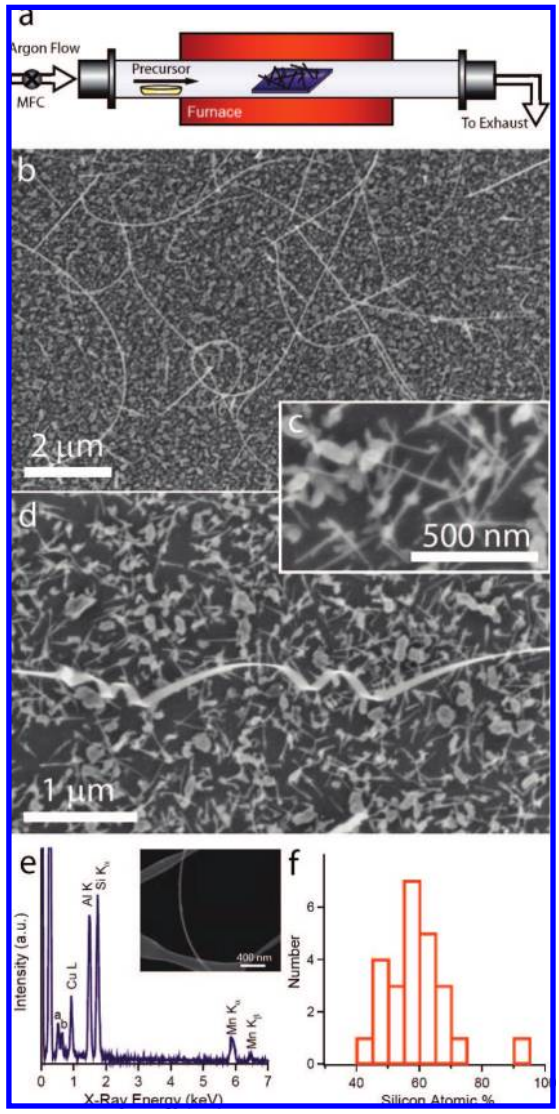

Figure 3. (a) Schematic CVD setup for manganese silicide nanowire growth. Representative scanning electron micrograph showing (b) nanowires and nanoribbons on the growth substrate, (c) shorter nanorods in the background, and (d) a twisting nanoribbon on the surface. (e) Representative EDS spectrum for a single 1-D nanostructure (shown in the inset). Peaks labeled a and b are O K_α and Mn $L_{\alpha 1}$ peaks, respectively. (f) Histogram of Si atomic percentage for 25 individual nanowires as measured by EDS.

small nanoparticles were observed with much higher density. Our observations suggest that all nanowires, nanoribbons, and nanorods nucleate from these particles. Nanowires and ribbons also sometimes appear to be "decorated" with secondary particles.

To reveal their elemental composition, nanowires and nanoribbons were dispersed on copper grids and analyzed using EDS. This process preferentially favors the deposition of the longer nanowire and nanoribbon morphologies over the shorter nanorods. Additionally, once these longer nanostructures have been processed, differentiation between nanowires and nanoribbons becomes nearly impossible as the twisting morphology of nanoribbons, which reveals their differential width, is usually lost during processing. As a result the following characterization focuses on the analysis of a mixture of the nanowires and nanoribbons, but for simplicity, these structures will be loosely referred to as "nanowires" (NWs) for the rest of the discussion. Individual NWs (25) were analyzed for Si and Mn atomic concentration using this method as shown in a representative spectrum (Figure 3e). The copper and aluminum peaks arise from the copper sample grid and aluminum sample holder, and the carbon observed in the sample is caused by *in situ* electron beam mediated carbon deposition. The other peaks can be identified as arising from Mn and Si. The spectra were quantitatively analyzed to determine the ratio of Mn to Si in the nanowires. A histogram of the percentage of Si determined from each spectrum (Figure 3f) shows the average Si atomic composition of the 25 nanowires analyzed was $58 \pm 11\%$, with a wide variability. One nanowire appeared to be nearly completely silicon. Usually NWs which were more heavily decorated with particle growth tended to have a higher Mn concentration. We suspect that in such NWs the observed composition is artificially Mn-rich due to these surface growths.

Nowotny Chimney Ladder Structures. To understand the HRTEM and identify the phases, we need to revisit the NCL crystal structures of the specific HMS compounds in greater detail. These structures are composed of a tetragonal sublattice of Mn atoms and a tetragonal sublattice of Si atoms the length of which are defined by the helix repeat units shown schematically in Figure 1a. The two sublattices are not necessarily themselves commensurate; their periodicity along the *c* axis direction of the full unit cell, c_{Mn} and c_{Si} for Mn and Si sublattices respectively, have an approximate relationship of $c_{Si} \approx 4\, c_{Mn}$ as shown in Figure 1a. However, every commensurate $MnSi_{2-x}$ unit cell must contain an integer number of each of the sublattices in one unit cell to produce a repeating crystallographic unit, i.e.:

$$c = nc_{Mn} = mc_{Si} \tag{1}$$

where *n* and *m* are integers representing the number of sublattices of Mn (*n*) and Si (*m*) present in the unit cell. c_{Mn} is nearly constant among different HMS phases, but there is some slight variation in c_{Si}, giving rise to a wide variety of NCL structures with *c* unit cell lengths up to tens of nanometers (such as shown in Figure 1e). Because the removal of *m* evenly spaced silicon atoms from a perfect parent structure of Mn_nSi_{2n} (vide infra) should result in the creation of *m* subcells, it can be argued and also empirically shown that the NCL structures of HMS have the general formula Mn_nSi_{2n-m}.

The NCL structures are sometimes dubbed a "defect" structure of the parent $TiSi_2$ due to the "missing" Si atoms in the daughter NCL structures.[6,18] $TiSi_2$ is a nearly tetragonal, orthorhombic structure with chimneys of Ti atoms and zigzagging Si ladders (Figure 1b). It is sometimes described by stacked sheets of pseudohexagonal 6^3 nets (a net of 6 sided polygons with 3 polygons touching at vertices) of Si atoms each pseudohexagon containing a Ti atom, giving 3^6 nets (a net of triangles with 6 such polygons meeting at a vertex) with respect to Ti atoms. These nets are clearly visible when viewed along the [001] axis of $TiSi_2$ as shown in Figure 1b. Similar, though distorted, versions of such nets are seen along the [110] axis of NCL HMS structures. The missing Si atoms in the NCL structures, relative to the parent structure, give rise to relaxation of the Si sublattice, though the Mn sublattice shows little relaxation. This relaxation gives rise to an apparent rotation of the stacked sheets in the NCL structures.[18] Figure 1c shows a comparison of a $TiSi_2$ supercell with a supercell of the relatively simple HMS compound Mn_4Si_7. This superstructure is clearly visible as a modulation in the contrast of HRTEM images of HMS samples and can be used for phase identification of the NCL phase as discussed in a later section.[12]

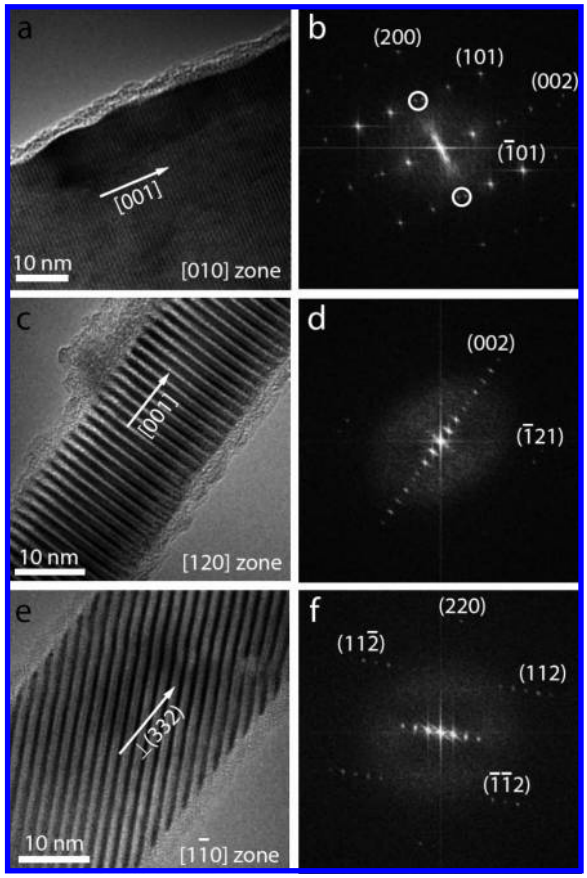

Figure 4. Transmission electron micrographs of three representative $MnSi_{2-x}$ nanowires in the (a) [010], (c) [120], and (e) [1$\bar{1}$0] zones and the corresponding indexed fast Fourier transform (FFT) of the images (b, d, f). The bands in c and e are attributed to the *c*-axis long-range ordering caused by mismatches in the Mn and Si sublattices. Circles in b indicate double spots due to Mn and Si subphase mismatches. The crystallographic index scheme is based on the Mn sublattice along the *c* axis.

High Resolution TEM Imaging of Nanowires. Representative lattice-resolved HRTEM images (Figure 4a,c,e), and their corresponding fast Fourier transforms (FFTs) (Figure 4b,d,f) of individual NWs show they are perfect single crystals, but with some unusual features. The HRTEM along the [010] zone axis (Figure 4a) seemingly shows "typical" lattice fringes, while HRTEMs along [120] (Figure 4c) and [1$\bar{1}$0] zone axes (Figure 4e) display clear long-range order along the *c*-direction of the crystal lattice as contrast modulation bands several nanometers in width in addition to lattice fringes.[12] Fast Fourier transforms (FFT) of these images (Figure 4b,d,f) have many closely spaced spots along the crystallographic *c* direction and also reveal interesting spacing anomalies. These FFTs (and every NW observed using the HRTEM) can be indexed to a tetragonal unit cell as labeled, consistent with the basic tetragonal NCL $MnSi_{2-x}$ structure. These atypical HRTEM images and FFTs (and electron diffraction patterns discussed later) are the consequence and signature of the mismatched sublattices of intricate $MnSi_{2-x}$ NCL structures. Each bright "main" spot, associated with diffraction from the Mn sublattice (c_{Mn}), is superimposed with a series of more closely spaced "satellite" reciprocal spots, associated with a larger Si sublattice (real space) spacing (c_{Si}). Following convention[12] we are indexing NCL HMS diffraction patterns to the Mn sublattice because the Mn sublattice does not change appreciably among the different HMS structures. Therefore, crystal directions and planes mentioned are all relative to the Mn sublattice. Because the "main" spots and "satellite" spots are associated with diffraction from the two different sublattices in the HMS structures one can determine that $a = 5.52$ Å (5.5251 Å, reported value), $c_{Mn} = 4.37$ Å (4.36583 Å), $c_{Si} = 17.09$ Å (17.4633 Å);[7] however, it is not so straightforward to determine the overall *c* and hence the subphase directly. Each HMS NCL structure has a Si sublattice which is slightly different in size so this variation in Si sublattice size in theory can be used to identify the actual NCL phase based upon the match or mismatch of the satellite peaks from different main spots. Unfortunately, the FFTs obtained do not have the resolution necessary to allow an accurate measurement of this mismatch. NWs were observed to grow along the [001] direction as well as perpendicular to (332) and (321) planes. These different growth axes are clearly expressed by the different orientation of the contrast modulation bands relative to the growth axis in HRTEM images (Figure 4a, c, and e). All nanowires are coated with 2−3 nm of amorphous material, which is well attributed to SiO_2 due to the self-oxidation of silicides.[60]

It is clear from the EDS spectra and HRTEM data that these NWs have the NCL structures of the HMS. However, neither EDS nor TEM is adequate to enable distinction between the many possible NCL structures. PXRD of the as-grown substrates was also attempted, but the small quantities of deposited material on nanowire laden substrates did not provide enough intensity for analysis. Substrates which experienced conditions favoring thin film deposition were also analyzed revealing diffraction patterns easily recognized as due to HMS, but phase differentiation could not be achieved due to nearly identical diffraction peaks between different NCL structures up to high angles. However, careful determination of the exact phase is highly desirable to help clear up the confusing disparity in reported physical properties of HMS structures.

Phase Identification of NCL Structures. For simplicity we follow a method developed by H. Q. Ye and S. Amelinckx[12] for identifying the HMS NCL phases of thin film samples using selected area electron diffraction (SAED) which relies on the particular sublattice structure of NCL phases and assumes a commensurate HMS crystal structure. The major distinction between the different NCL Mn_nSi_{2n-m} structures is the size of the Si sublattice cell along the unique *c* axis of the unit cell, c_{Si}, which gives rise to variation in the size of the *c* lattice constant, as dictated by the relationship $c = nc_{Mn} = mc_{Si}$ (eq 1). One might imagine that measuring c_{Mn} and c_{Si} directly could allow subphase identification, but the subtle difference in c_{Si} makes this in practice quite difficult. The slight differences in c_{Si} also manifest themselves in the electron diffraction patterns of the HMS structures as the mismatched satellite peaks and the resulting "spacing anomaly" seen in ED (and the FFTs above) can allow a more sensitive and accurate differentiation. This strategy is similar to the use of the Vernier effect to accurately measure small distances with a caliper.

Because the only difference between various NCL phases lies in the *c* parameters of their unit cells and Si sublattice cells, ED patterns along zone axes that are perpendicular to the *c* axis will be required to observe the differences. Among such zone axes, lower index [100], [110], and [120] are the most useful, as the satellite spots arising from different main spots do not generally overlap. Figure 5a illustrates a schematic ED pattern

(60) Rebien, M.; Henrion, W.; Angermann, H.; Teichert, S. *Appl. Phys. Lett.* **2002**, *81*, 649–651.

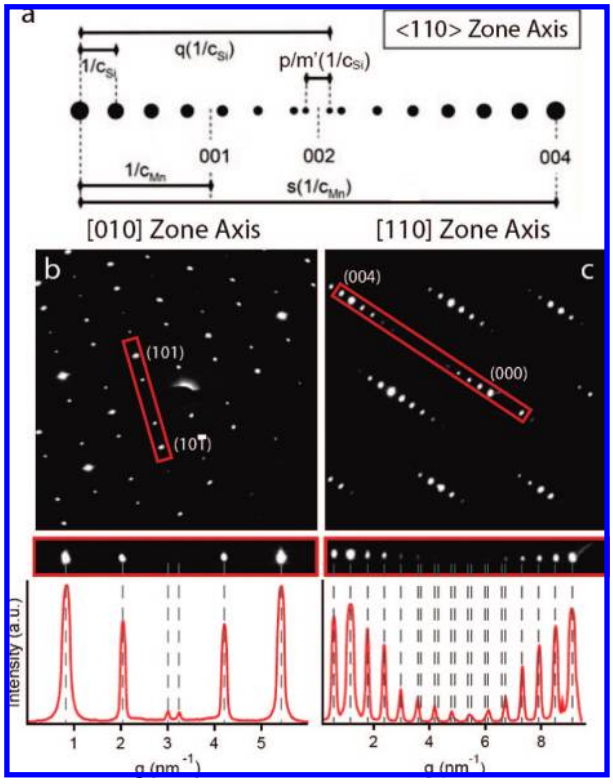

Figure 5. (a) Schematic drawing of ⟨110⟩ zone axes labeling important reciprocal space distances important for phase identification. (b) Subphase identification of $Mn_{19}Si_{33}$ nanowires from select area electron diffraction patterns showing original SAED patterns, magnified regions of interest, and linescans through regions of interest for [010] zone axis (b) and the [110] zone axis (c). Dashed gray lines on line scans show predicted locations for spots in a $Mn_{19}Si_{33}$ NCL structure.

along the ⟨110⟩ zone axis that is again indexed based on the Mn sublattice. This schematic clearly shows two large main spots each superimposed by regularly spaced smaller satellite spots. Note that the satellite spots arising from the different main spots do not overlap in the center. The large main spots in this diagram arise from diffraction from the Mn sublattice so the distance between them will be some multiple of the reciprocal Mn sublattice spacing, s ($1/c_{Mn}$) (Figure 5a). The value of integer s depends on the extinction of different diffraction spots along different zone axes and is either 2 or 4 for the zone axes [100] and [110], respectively. Alternatively, one could describe the distance between these main spots in terms of the reciprocal silicon sublattice spacing ($1/c_{Si}$); to pass the center point between the two main spots, q ($1/c_{Si}$) is needed, where integer q is the number of reciprocal silicon sublattice spacings required (Figure 5a). The value of q is either 4 or 8 depending on the zone axis under study. From measuring q ($1/c_{Si}$) from each main spot from both directions, it is clear that adding these q ($1/c_{Si}$) values together to obtain the distance between the main spots would result in double counting the small mismatch region in the center. This mismatch region is a fraction of the reciprocal silicon sublattice spacing and can be expressed as p/m' ($1/c_{Si}$), where p and m' are both integers. Thus the distance between the two main spots can now be expressed as

$$\left(2q - \frac{p}{m'}\right)\left(\frac{1}{c_{Si}}\right) = s\left(\frac{1}{c_{Mn}}\right) \tag{2}$$

Rearranging this equation and substituting into eq 1 reveals

$$\frac{c_{Mn}}{c_{Si}} = \frac{m}{n} = \frac{sm'}{2qm' - p} \tag{3}$$

Eq. (3) relates the mismatch $(p/m')(1/c_{Si})$ to the ratio c_{Mn}/c_{Si} and it can be shown (detailed derivation in the Supporting Information) that

$$m = sm' \text{ and } n = 2qm' - p \tag{4}$$

which directly determines m and n identifying the HMS subphase Mn_nSi_{2n-m}. Each individual commensurate NCL HMS phase reported to date has a unique mismatch, since each one has a unique c_{Si}, for a given zone axis (the mismatch may differ by a simple factor between different zone axes) (see Table S6). Furthermore, juxtaposition of the simulated electron patterns (Tables S7−S9) clearly shows that they can be readily differentiated by simple pattern recognition.

Identification of the $Mn_{19}Si_{33}$ NCL Phase Using SAED Analysis. Following the procedures outlined above, we have carefully acquired and analyzed SAED patterns of nanowires to determine the NCL HMS phase produced, with two examples shown in Figure 5b,c. The ED spots are usually very close to each other due to the large real space spacings; therefore long camera distances with careful calibration must be employed. It should be noted that analysis of these diffraction patterns requires careful identification of the main spots. The assumption that the brightest spots in the pattern are the main spots arising from Mn sublattice diffraction is not always true, as double diffraction may cause satellite spots to be brighter than their associated main spots.[11] Instead, the identification of main spots is made by measuring the reciprocal space distance of a suspected main spot from the zero beam and other neighboring main spots and verifying the expected reciprocal space distances. To accurately obtain peak positions, intensity linescans along the satellite axes are obtained from the digital image and the peaks are fit to Gaussian functions. The satellite peaks are then labeled, and the average separation between many pairs of satellite peaks is used to determine $1/c_{Si}$. The mismatch in the center can then be measured relative to the measured $1/c_{Si}$; the resultant value is the factor p/m'.

As an example, an SAED pattern of a nanowire along the [010] zone axis is shown in Figure 5b. The area enclosed in the red box is highlighted to show the main spots, indexed in the larger pattern, along with a series of satellite spots. The lower panels of Figure 5b,c shows the intensity linescans superimposed with the predicted peak locations (dashed lines) based on the presumed $Mn_{19}Si_{33}$ phase. The average value of $1/c_{Si}$ is obtained (as previously described) taking into account that along the [010] zone satellite spots are separated by $2(1/c_{Si})$. Finally, the mismatch between the centermost spots relative to $1/c_{Si}$, i.e., the value p/m', was found to be 0.398. This corresponds well to the predicted mismatch of $Mn_{19}Si_{33}$ (0.4) and distinctly different from the predicted (p/m') values of other HMS subphases, therefore discreetly identifying the specific NCL phase of this NW.

Such SAED experiments and analyses are nontrivial. Among the three different nanowires from the same sample that have been completely analyzed so far, the subphase was always identified to be $Mn_{19}Si_{33}$. Thus it seems likely that a given sample produces only one subphase of nanowires; although, further work is necessary to rule out the formation of mixtures of subphases. Curiously, this $Mn_{19}Si_{33}$ phase has not been identified via single crystal X-ray diffraction for a pure manganese silicide in bulk but has been observed in previous

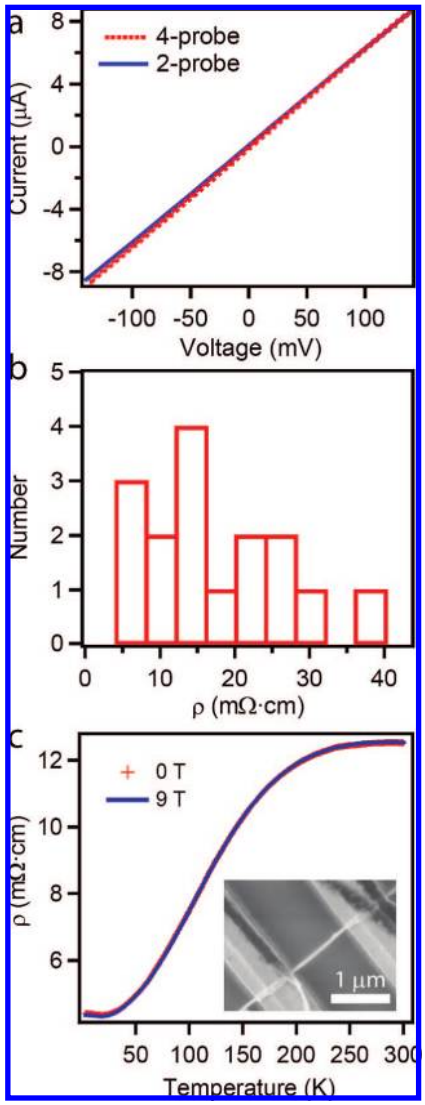

Figure 6. Electrical properties of $Mn_{19}Si_{33}$ nanowires or nanoribbons. (a) $I-V$ curves of an individual 2-probe and 4-probe device of $Mn_{19}Si_{33}$ nanowire contacted with Ti/Au electrodes. (b) Histogram of calculated resistivities based on 16 individual 4-probe devices. (c) Resistivity measured as a function of temperature for a representative 2-probe device at the applied magnetic fields of 0 and 9 T. Inset shows a representative 2-probe nanowire device.

TEM explorations,[12] and this specific structure type in bulk has also been seen previously in ternary NCL phases.[6]

Electrical Properties of $Mn_{19}Si_{33}$ Nanowires. Single-nanowire devices were fabricated with $Mn_{19}Si_{33}$ NWs via standard electron-beam lithography for electrical transport studies. Contact to nanowires was made using evaporated lines of titanium and gold. All devices measured were ohmic in character as shown in the representative $I-V$ curve (Figure 6a). Resistivity was estimated for 16 4-probe nanowire devices, assuming cylindrical nanowire morphology in each case, giving an average estimated resistivity of 17.4 mΩ·cm with a standard deviation of 9.7 mΩ·cm (histogram shown in Figure 6b). It was clear from comparison of 4-probe (23.6 mΩ·cm) and 2-probe (26.3 mΩ·cm) measurements (Figure 6a) that contact resistance was minimal in these devices. Back-gating of these devices showed no field effect on the device conductivity. The ohmic character and lack of gating behavior are in agreement with electrical measurements on bulk samples, which are known to be degenerately doped p-type seminconductors.[20] Reported resistivity values for $MnSi_{2-x}$ single crystalline and thin film samples have a very large variation of 0.37−100 mΩ·cm.[61] Variability in reported resistivities may arise from many sources including poor sample quality with very few reports fully characterizing the subphase of samples. Inclusion of MnSi crystallites is often reported in melt grown crystals,[62] but vapor phase grown single crystals without such deficiencies have been reported.[63] Furthermore, $MnSi_{2-x}$ single crystals show anisotropic resistivities along different crystallographic directions with differences as high as a full order of magnitude,[64] with the higher resistivities found along the *c* axis. The large standard deviation in resistivity observed in our case may in part be due to the unrealistic, but arguably unavoidable, assumption that the nanowires are cylindrical, given that the morphology is a mixture of wires and ribbons. However, since we have observed multiple growth directions in our vapor-grown nanowires and nanoribbons, anisotropic resistivity is the most likely contributor to the observed variation.

Additionally, we have investigated the temperature dependence of the resistivity for a number of $Mn_{19}Si_{33}$ NWs using 2-probe devices from 5 to 300 K. A representative trace (Figure 6c) shows monotonically increasing resistivity with increasing temperature, in agreement with reported measurements completed on single-crystalline and thin film samples.[20,61] The observed metallic character of the resistivity under the temperature range studied is in agreement with a semiconductor operating in the extrinsic regime at room temperature. The resistance under applied magnetic fields (Figure 6c) shows that the magnetoresistance of $Mn_{19}Si_{33}$ NWs never exceeds more than 1%. Many manganese silicides are magnetic; however, the magnetism of HMS phases has rarely been examined due to the difficulty in matching the specific phase with the magnetic properties.[65] For the basic Mn_4Si_7 phase previously studied, the magnetization saturation was found to be only 0.012 μ_B/Mn for this weak itinerant electron system,[65] which likely implies low magnetoresistance. The electrical properties of the $Mn_{19}Si_{33}$ NWs are in agreement with reports on both bulk and thin film samples of generic HMS compounds. These results are promising for the thermoelectric properties of $MnSi_{2-x}$ NWs in that the electron conductivity of these semiconducting silicide nanowires is not affected by their size, while thermal conductivity of the nanowires can be reduced due to nanostructures, thereby increasing *ZT*.

Chemical Vapor Deposition Synthesis of $Mn_{19}Si_{33}$ Nanowires. It is clear from this structural and physical property characterization that the nanowires and nanoribbons we have synthesized are HMS, but a number of mechanistic questions are still unanswered. The growth of HMS nanowires requires control of material delivery and phase formation as well as a mechanism promoting anisotropic 1-D growth. The mechanism favoring the growth of $Mn_{19}Si_{33}$ NWs over a thin film in the CVD process herein is not clear. In previous TMS NW syntheses via SSP-CVD[38,39,41] a thin layer (1−2 nm) of SiO_2 on Si substrates was required for efficient NW growth, while using H-terminated Si substrates or substrates with thicker oxide films favored TMS film growth without NW nucleation. However, in the case of $MnSi_{2-x}$ NWs no thin film of oxide is

(61) Hou, Q. R.; Chen, Y. B.; He, Y. J. *Mod. Phys. Lett. B* **2006**, *20*, 877–886.
(62) Kawasumi, I.; Nishida, I.; Masumoto, K.; Sakata, M. *Jpn. J. Appl. Phys* **1976**, *15*, 1405–6.
(63) Kojima, T.; Nishida, I. *Jpn. J. Appl. Phys* **1975**, *14*, 141–2.
(64) Zaitsev, V. K. Thermoelectric Properties of Anisotropic $MnSi_{1.75}$. In *CRC Handbook of Thermoelectrics*; Rowe, D. M., Ed.; CRC Press: Boca Raton, FL, 1995; pp 299−309.
(65) Gottlieb, U.; Sulpice, A.; Lambert-Andron, B.; Laborde, O. *J. Alloys Compd.* **2003**, *361*, 13–18.

required to nucleate NWs; in fact the use of H-terminated substrates or thick oxides results in similar growth behavior as when a thin oxide is used. We immediately looked for and have preliminarily ruled out two fundamental NW growth mechanisms: screw-dislocation driven and vapor−liquid−solid (VLS) nanowire growth. The growth of PbS nanowires through a screw dislocation driven mechanism was recently reported,[66] but preliminary investigations do not suggest that $MnSi_{2-x}$ NWs are grown in this fashion. Investigation of numerous HMS nanowire and nanoribbon samples using SEM and TEM have not revealed any particles of distinctively different material visible on their tips, the hallmark of most VLS and vapor−solid−solid (VSS) NW growth.[67] However, NWs always seem to nucleate from "islands" on the surface, presumably HMS themselves as revealed by PXRD of thin film samples. It is possible, therefore, that $MnSi_{2-x}$ NWs grow via a VSS process with the catalyst particles remaining on the substrate surface. Another option is that Si NWs are being synthesized and silicided during the growth process. The rare but present Mn-rich surface deposits and the observation of a nearly all silicon nanoribbon by EDS would support this mechanism and could also account for the discrepancy in the Mn and Si content in the NW and precursor. At this time, it is not clear why the growth mechanism allows for both NW and nanoribbon morphologies. Further study is needed to answer these questions.

Questions also remain on the formation of the specific HMS phase for these NWs. It is curious that the nanomaterial product has a Mn/Si composition ratio of ~1:1.75 while the $Mn(CO)_5SiCl_3$ precursor delivered has a predefined Mn/Si ratio of 1:1. Furthermore, the HMS NWs produced are not the silicide phase one would expect (Mn_5Si_3 is) based on the "first phase rule" of silicide phase formation between metal thin films and silicon.[68] The first phase rule, an empirical rule based on thermodynamic and kinetic considerations, states that in the interfacial reactions of silicon with a transition metal the first phase to form is the highest melting point congruently melting species nearest the lowest temperature eutectic in the phase diagram.[68] Admittedly, the NW reaction at hand is different from the interfacial thin film reactions, and nanomaterial formation is by definition a kinetically controlled process. Additionally, the thermal decomposition pathway of $Mn(CO)_5SiCl_3$ has not been well established, which can have an influence over the stoichiometry of the resulting CVD products. It is possible that the precursor first undergoes some reaction either in gas phase or on the substrate surface which yields intermediate fragments with different elemental ratios before incorporation into solid products. Mass spectrometry investigation of the SSP could shed some light on such possibilities. The substrate could also contribute the additional silicon in the NW product. We note that most other TMS nanowire syntheses which do not use the SSP approach had to explicitly rely on the growth substrate as the source of Si[48,56,58] or the transition metal.[52]

An even more interesting question is whether NWs of other HMS phases besides $Mn_{19}Si_{33}$ can be synthesized. One might imagine that the thermodynamic difference between all these phases must be quite minute. To date we have only found $Mn_{19}Si_{33}$, but further studies are required to verify whether our samples are purely $Mn_{19}Si_{33}$ or a mixture of subphases. It would be fascinating to observe NWs of other homologous NCL HMS phases and even more challenging to potentially even synthesize other HMS nanowires controllably, as that would allow systematic studies of the differences in physical properties between the HMS phases.

Conclusion

We have reported the first synthesis of nanowires and nanoribbons of semiconducting higher manganese silicides, a Nowotny chimney ladder phase, using CVD of the single source precursor $Mn(CO)_5SiCl_3$. Scanning electron micrsocopy of as grown substrates revealed long 1-D nanowires and nanoribbons and shorter nanorods accompanied by nanoparticles on the substrate surface and occasionally decorating the nanowires. The long nanowires and nanoribbons were analyzed by EDS spectroscopy and HRTEM revealing them to be higher manganese silicides. Using careful SAED analysis we have identified the specific phase of the synthesized HMS nanowires and nanoribbons as $Mn_{19}Si_{33}$, one of the complex commensurate HMS NCL structures which have been traditionally described as a series of distinct commensurate lattices containing two different sublattices one each for the transition metal atoms and main group elements. We have presented our results in the conceptually simpler commensurate construct although the more general incommensurate description could be more versatile and accurate for future discussion of complex NCL nanostructures. This development further expands the growing toolbox for nanomaterial synthesis of intermetallic compounds and brings together the nanometer length scales reached by both the crystalline structures of complex intermetallic phases and the physical size of nanomaterials. Electrical characterization showed that these 1-D nanomaterials are degenerately doped and that the resistivity of bulk and thin film counterparts is maintained in the 1-D morphology. Further studies to measure the Seebeck coefficient and thermal conductivity are underway for this promising nanoscale thermoelectric material which integrates both major thrusts in the development of new thermoelectric materials, complex crystal structures and nanoscale dimensions. Though the exact growth mechanism of these silicide nanowires and nanoribbons remains to be understood, this successful first synthesis of 1-D nanomaterials of the semiconducting Nowotny chimney ladder compounds will enable the fundamental investigation of phonon confinement and phonon transport and open up new opportunities for the study of complex materials at the nanoscale.

Acknowledgment. This research was supported by an IEDR grant, the startup fund provided by UW-Madison, and Research Corporation through a Cottrell Scholar Award. S.J. also acknowledges the 3M Nontenured Faculty Award and a DuPont Young Professor Grant for support. J.M.H. is partially supported by a Merck Research Laboratories Fellowship. The authors would also like to thank Dr. Alex Kvit for assistance with the SAED.

Supporting Information Available: Details of the X-ray crystal structure determination of precursor $Mn(CO)_5SiCl_3$ and the details of the higher manganese silicide subphase identification method, including full details of mathematics and tabulation of various phases. This material is available free of charge via the Internet at http://pubs.acs.org.

JA8065122

(66) Bierman, M. J.; Lau, Y. K. A.; Kvit, A. V.; Schmitt, A. L.; Jin, S. *Science* **2008**, *320*, 1060–1063.
(67) Persson, A. I.; Larsson, M. W.; Stenstrom, S.; Ohlsson, B. J.; Samuelson, L.; Wallenberg, L. R. *Nat. Mater.* **2004**, *3*, 677–681.
(68) Walser, R. M.; Bene, R. W. *Appl. Phys. Lett.* **1976**, *28*, 624–625.